










RESEARCH ARTICLE | OCTOBER 17 2024

A thorough experimental assessment of THz-TDS plasma diagnostic techniques for nuclear fusion applications

G. Galatola Teka ; K. Peng ; M. Alonzo ; F. Bombarda ; C. L. Koch-Dandolo ; L. Senni ;
A. Taschin ; M. Zerbini  



Rev. Sci. Instrum. 95, 103519 (2024)

<https://doi.org/10.1063/5.0237745>



View
Online



Export
Citation

Articles You May Be Interested In

Radiative precursors driven by converging blast waves in noble gases

Phys. Plasmas (March 2014)

W-band tunable, multi-channel, frequency comb Doppler backscattering diagnostic in the ASDEX-Upgrade tokamak

Rev. Sci. Instrum. (August 2023)

Electron cyclotron emission spectra in X- and O-mode polarisation at JET: Martin-Puplett interferometer, absolute calibration, revised uncertainties, inboard/outboard temperature profile, and wall properties

Rev. Sci. Instrum. (September 2016)



Special Topics Open for Submissions

[Learn More](#)

A thorough experimental assessment of THz-TDS plasma diagnostic techniques for nuclear fusion applications

Cite as: *Rev. Sci. Instrum.* **95**, 103519 (2024); doi: [10.1063/5.0237745](https://doi.org/10.1063/5.0237745)

Submitted: 6 September 2024 • Accepted: 9 September 2024 •

Published Online: 17 October 2024



View Online



Export Citation



CrossMark

G. Galatola Teka,¹  K. Peng,²  M. Alonzo,¹  F. Bombarda,¹  C. L. Koch-Dandolo,^{3,a)}  L. Senni,^{1,b)} 
A. Taschin,^{1,c)}  and M. Zerbini^{1,d)} 

AFFILIATIONS

¹ ENEA, Nuclear Department, C. R. Frascati, Via E. Fermi 45, 00044 Frascati (Roma), Italy

² Department of Physics, Clarendon Laboratory, University of Oxford, Parks Road, Oxford OX1 3PU, United Kingdom

³ Centro de Investigaciones en Optica A.C., Loma del Bosque 115, Lomas del Campestre, Leon, Guanajuato 37150, Mexico

^{a)} Present address: SUPSI University, Le Gerre, via Pobiette 11 CH-6928 Manno.

^{b)} Present address: CNR - IAC, Via dei Taurini, 19, 00185 - Roma - Italy.

^{c)} Present address: CNR - Ist. Naz. Ottica, Via Carrara 1, 50019 S. Fiorentino (FI).

^{d)} Also at: Department of Physics, University of Oxford UK.

Author to whom correspondence should be addressed: marco.zerbini@enea.it

ABSTRACT

In this paper, the study of a plasma diagnostic system based on the THz time domain spectroscopy technique is presented. Such a system could potentially probe a large part of the electromagnetic spectrum currently covered by several other diagnostics in a single measurement. This feature, keeping in mind the basic requirements for plasma diagnostics in nuclear fusion experiments, such as robustness and hard environment applicability, as well as durability and low maintenance, makes the diagnostic of great interest. A conceptual design of the THz-TDS diagnostic has been developed, starting from the well-established classical microwave and far infrared plasma diagnostics landscape. The physical constraints and required instrumental characteristics have been studied and are described in detail here, together with the solutions available for each type of plasma measurement. Specific experimental laboratory tests of the different experimental configurations have been carried out, evaluating the capacity and potential of the novel diagnostic, together with the instrumental constraint, within the diagnostic parameter space.

© 2024 Author(s). All article content, except where otherwise noted, is licensed under a Creative Commons Attribution-NonCommercial-NoDerivs 4.0 International (CC BY-NC-ND) license (<https://creativecommons.org/licenses/by-nc-nd/4.0/>). <https://doi.org/10.1063/5.0237745>

I. INTRODUCTION

The electromagnetic spectrum between microwaves and mid-infrared light is currently defined as the terahertz band (1 THz = 10^{12} Hz, corresponding to 0.3 mm wavelength), a spectral region where electronic and optical technologies overlap. Over the years, the word “terahertz” became a moniker encompassing the entirety of this large spectral region, which ranges from 0.3 to 30 THz, for which many interesting applications appeared to be possible. For the scope of this paper, we focus on the opportunity offered by THz Time Domain Spectroscopy (TDS) for plasma diagnostics applications¹ in nuclear fusion.² The fortunate landscape of the optical

properties of plasma in the lower part of the THz spectral region, traditionally called Far Infrared Radiation (FIR), has spawned a class of exceptionally successful diagnostics for magnetic confinement plasma devices, such as tokamaks, since the early days of experimental plasma physics. FIR diagnostics use a combination of optical and electronic techniques, often using the same instrument.^{3–5} More recently, the opportunities offered by THz-TDS technology have raised a high level of interest in the diagnostic potential of this technique.^{6–8} In particular, the wide spectral range of modern terahertz sources,^{9,10} detection speed, possibility of using optical fibers to carry the laser beam to the THz emitter and receiver^{11,12} for tens of meters, and ease of access to tokamak plasmas make it a

very good candidate to potentially replace a number of traditional fusion plasma diagnostics, such as interferometry, reflectometry, and polarimetry,¹ with one single multi-functional instrument.^{13,14}

Complications and difficulties are in no short supply. THz measurements in plasma physics and nuclear fusion environments will be significantly different from those in laboratory applications, which have been successful in recent years. To start, the “sample” is a plasma device of macroscopic size, not a fragment of material easily handled and positioned. The weakness of the THz signals is another major difficulty, given the low power of THz sources¹⁰ (μW), long optical paths, and heavy dispersion in nuclear fusion experiment plasmas. The critical alignment between the detector and emitter and the polarization issues will require a thorough optical design of long range THz optics to achieve the required measurement precision signal-to-noise ratio (SNR) while maintaining the temporal resolution, which is the time required for a single measurement, compatible with the time scale of the plasma physics experiments (a few milliseconds). The remainder of this paper is organized as follows: in Sec. II, the basic concepts of THz-TDS are presented. Section III is concerned with the principles of FIR and submillimeter wave plasma diagnostics (interferometry, polarimetry, and reflectometry); then in Sec. IV, the design principles of the foreseeable THz-TDS plasma diagnostics are described with particular attention to tokamaks.^{15,16} The conceptual design of the THz-TDS multi-functional diagnostic system is described in Sec. V, and in Sec. VI we present a series of targeted laboratory tests that cover most of the experimental issues and constraints of the method. Finally, Sec. VII is devoted to the discussion and an outline of future work. The results are based on a series of experiments performed over time in collaboration between ENEA Frascati, Clarendon Laboratory at Oxford University (UK), and Centro de Investigación Óptica (CIO, Leon, Mexico), specifically devoted to the realization of the diagnostic. The International System of Units (SI) will be used throughout this paper.¹⁷

II. THz-TDS SPECTROMETRY BASIS

The THz-TDS technique is now applied in many scientific and engineering areas, such as semiconductors, materials and components characterization, biophysics, and medicine.¹⁸ Since it is broadly described in the literature, the details will not be repeated in this paper. Let us just recall the basic principles: the interaction of femtosecond infrared laser pulses ($\lambda \sim 790$ nm, duration

<100 fs, repetition rate ~ 100 MHz) with a photoconductive plate (for example, GaAs) is routinely used to generate extremely broadband (100 GHz up to 10 THz) single-cycle THz pulses with a typical duration between 2 and 3 ps through a process first observed by Auston, called “photoconductive generation of terahertz radiation.”⁹ Such short transients contain as few as one cycle of the electric field oscillation, thus producing the aforementioned broad spectral range: either the THz or the mid-infrared ranges can be covered in their entirety, depending on the choice of the emitter.¹⁹

THz pulses can be coherently detected with very high sensitivity either with photoconductive^{20,21} or electro-optical²² (EO) detection systems. The main laser beam is split into two branches, one to drive the emitter and the other to synchronously enable the detector to take in the pulse only when the emitter is on, thereby increasing the SNR. The path difference between the emitter and detector is scanned by recording the THz pulse amplitude at each given position x of the scanner, providing a time delay of $t = x/c$ (c is the speed of light in a vacuum) thereby reconstructing (or mapping) the full pulse vs time. In addition, the emitter bias is modulated at a much lower frequency (~ 20 kHz) to increase the SNR using lock-in techniques. To properly design a THz-TDS experimental setup for each specific purpose, it is important to obtain an overview of the different timescales involved in the process and their interconnection and significance, which are summarized and compared in Table I. The pump laser pulse width is narrower than that of the generated THz pulse owing to the nature of the process, but the repetition rate is the same. A path difference scan of 1.5 mm usually covers the THz pulse length extension ($t = x/c \sim 5$ ps). By increasing it, the spectral resolution can be improved, according to the spectroscopic Rayleigh principle.²³ The key condition for enabling the THz-TDS measurements is expressed by the following inequality:

$$\text{laser pulses interval} \ll \text{modulation time} \ll \text{scanning time.}$$

This means a slow scan time in relation to the modulation period; thus, with the scanner ideally fixed in a given position, the modulation signal runs across many cycles while many more THz pulses occur during one phase when the modulation signal is high, allowing a lock-in average. The fast scanning (~ 10 ms) required by plasma diagnostics for fusion experiments is maintained in the above inequalities. It should be noted that the temporal resolution is longer than that of a single scan because, to reach the desired SNR, it is often necessary to average many scans. In any case, the path difference scanning time must remain well above the

TABLE I. Schematic comparison of the relevant THz-TDS measurement timescales for a plasma diagnostic setup.

Quantity	Timescale	Pulses in half-modulation cycle	$\frac{\text{Timescale}}{\text{THz pulse}}$	Pulses in one path scan
Laser and THz rep. Rate	10 ns (100 MHz)	2500	2000	1 000 000
Emitter modulation (lock-in)	0.05 ms (20 kHz)	0.5	10^7	200
Path scanning time	10 ms	...	2×10^9	1
THz pulse duration	5 ps	...	1	...
Laser pulse duration	100 fs	...	2×10^{-2}	...
1 THz sine wave period	1 ps	...	0.2	10^{-8}

emitter voltage modulation to enable the lock-in amplifier average of the signal during a single scan. For a preliminary estimate of SNR in THz plasma measurements, we start from the basic assumption that averaging M synchronous measurements of the same physical quantity, the random noise is reduced by a factor $1/\sqrt{M}$, while the amplitude of the synchronous signal is, in principle, unchanged.²⁴ Using the standard values in Table I and assuming a duty cycle of the emitter modulation of 50%, the half period will contain 2500 pulses, and consequently the noise will be reduced by a factor of $\sqrt{2500} \approx 50$, an estimate acceptable for laboratory-grade equipment.

III. FIR AND SUBMILLIMETER WAVES PLASMA DIAGNOSTICS

As mentioned in the Introduction, important plasma properties can be inferred by measuring the dispersion, refraction, and reflection of the millimeter and submillimeter probe waves. The related diagnostic applications have been extensively discussed by many authors,²⁵ and a short summary is provided in the following. For a plasma immersed in a uniform magnetic field B , two fundamental frequency values are defined as follows:

$$\omega_{pe} = \sqrt{\frac{ne^2}{\epsilon_0 m_e}}, \quad \text{Plasma Electron Frequency,} \quad (1)$$

$$\omega_{ce} = \frac{eB}{m_e}, \quad \text{Electron Cyclotron Frequency,} \quad (2)$$

where e and m_e are the electron charge and mass, respectively, ϵ_0 is the permittivity of vacuum, and n is the plasma numerical density in particles/m³. The quantity ω in the above equations, although often called *frequency* in accepted scientific parlance, is strictly speaking a pulsation or radian frequency, conventionally used because it gives the equations a more elegant form. In practical applications, the actual frequency $f = \omega/2\pi$ is used. For a monochromatic probe wave of radian-frequency ω perpendicular to the magnetic field B , there are two propagation modes defined by the orientation of the wave electric field vector \vec{E} :^{1,4,25} (1) the Ordinary (O) mode, defined by $\vec{E} \parallel \vec{B}$, and (2) the eXtraordinary (X) mode, defined by $E \perp B$. By using the cold plasma approximation, valid in the majority of experimental cases, that is, neglecting the plasma pressure effects and considering only the electromagnetic interactions (Cairns²⁶, Sec. 4.2), the refraction index N_O for the Ordinary (O) mode is

$$N_O = \sqrt{1 - \frac{\omega_{pe}^2}{\omega^2}} \approx 1 - \frac{\omega_{pe}^2}{2\omega^2}, \quad (3)$$

where the approximate form is valid for probe frequency much greater than plasma frequency, $\omega \gg \omega_{pe}$, a choice that ensures acceptable accuracy for diagnostic purposes.⁴

For the eXtraordinary (X) mode, the refraction index N_X is

$$N_X = \sqrt{\frac{(\omega^2 - \omega_L^2)(\omega^2 - \omega_R^2)}{\omega^2(\omega^2 - \omega_{UH}^2)}}, \quad (4)$$

where ω_L and ω_R are the two X -mode cutoffs ($N_X = 0$), called left (–sign) and right (+sign), respectively,

$$\omega_{L,R} = \sqrt{\omega_{pe}^2 + 0.25 \times \omega_{ce}^2} \pm 0.5 \times \omega_{ce} \quad (5)$$

and ω_{UH} is a resonance (N_X diverging) called upper hybrid frequency,

$$\omega_{UH} = \sqrt{\omega_{pe}^2 + \omega_{ce}^2}. \quad (6)$$

Waves are reflected at cutoffs where the refractive index N vanishes and absorbed at resonances ($N \rightarrow \infty$). In the latter case, the local plasma re-emits according to the blackbody laws.²⁷ For completeness, a second hybrid resonance, the Lower Hybrid frequency (LH), should be mentioned. Nevertheless, because it ranges in the MHz region, well away from FIR, it will not be considered in the remainder of this discussion. The above equations open the door to many FIR and millimeter-wave plasma diagnostics in magnetic confinement devices, such as tokamaks, a plasma confinement device based on the combination of a toroidal magnetic field generated by an external coil and a poloidal magnetic field created by the current induced in the plasma ring by a core transformer. Figure 1 summarizes the tokamak configuration and arrangement of the most important FIR diagnostics. Ample and detailed descriptions of tokamak science are available in the literature.^{15,16}

Radial frequency profiles obtained from Eqs. (1)–(6) for typical tokamak parameters are shown in Fig. 2. They determine the FIR wave propagation inside the plasma. On this basis, many diagnostics have been developed and successfully used: Interferometry exploits the phase shift induced in the probing wave by plasma dispersion.

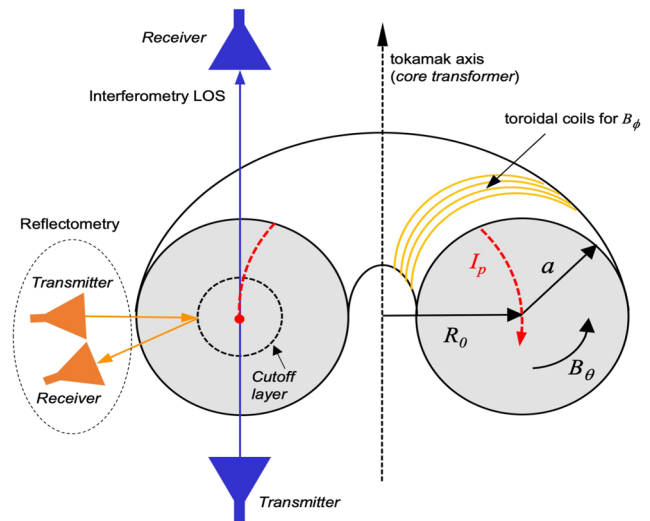


FIG. 1. Simplified schematic of tokamak configuration and FIR diagnostic arrangements. The major radius R_0 and minor radius a define the machine aspect ratio $A = \frac{R_0}{a}$: for JET¹⁶ $A = 3.1$, for DIII-D²⁸ $A = 4$, and for FTU²⁹ $A = 3.3$. The plasma current I_p , in red, is induced by the core transformer and, in turn, creates the poloidal field B_θ . The toroidal magnetic field B_ϕ is generated by the toroidal coil. The lines of sight (LOS) of the interferometer and reflectometer are indicated with the approximate position of the antennas.

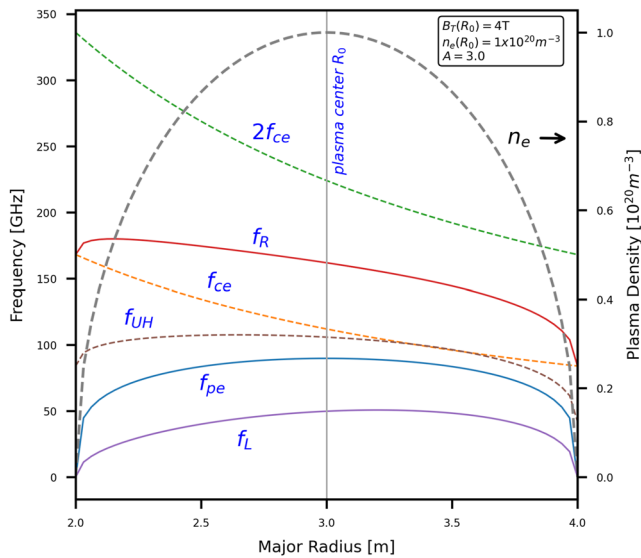


FIG. 2. Density profile (gray dotted line, right axis) and frequency profiles ($f = \omega/2\pi$, left axis) of electromagnetic wave cutoffs (solid lines) and resonances (dashed lines) for typical medium-size tokamak parameters. Center major radius $R_0 = 3.0$ m (vertical line), $B_0 = 4$ T, and peak density 10^{20} particles/m³. The relationships between cutoff and resonance values and position are of fundamental importance to optimize the diagnostic design and maximize plasma accessibility.

Polarimetry uses plasma birefringence properties to detect the polarization rotation of a FIR beam (Faraday and Cotton–Mouton effects), which can then be used to calculate the magnetic field strength. Reflectometry exploits beam reflection on plasma cutoffs to measure plasma density profiles and fluctuations. Electron Cyclotron Emission (ECE) diagnostic probes the electron temperature by means of blackbody plasma emission at the fundamental frequency in Eq. (2) and its integer harmonics, most important the second. The application of the THz-TDS technique to these diagnostics is discussed in Sec. IV.

IV. THE APPLICATION POTENTIAL OF THZ PLASMA DIAGNOSTICS

THz-TDS offers the unique possibility of directly measuring plasma properties through complete knowledge of the amplitude and phase information carried by the transmitted or reflected THz pulse. By detecting the arrival time of an electric field pulse after its interaction with the plasma, it is possible to determine the plasma refractive index and absorption coefficient (or equivalently the electrical conductivity) directly from the experiment. In addition, the two polarizations of the probing wave can be resolved simultaneously by using photo-conductive polarization-resolving detectors. The diagnostic capability of THz based TDS methods is also more far-reaching than that offered by frequency-domain techniques, such as Michelson interferometry, which is only sensitive to the field amplitude of radiation.³⁰

THz spectroscopy offers great potential for the evolution of diagnostic capabilities beyond the routine measurements of plasma density, and temperature, for the measurement of fluctuations,

charge density and conductivity, with unprecedented resolution and reliability. The first and more natural plasma diagnostic applications of THz TDS are interferometry,¹ polarimetry,¹ and reflectometry.^{1,4} **Interferometry** is the measurement of the plasma refractive index through the detection of the phase difference between a microwave beam of a suitable frequency traveling in the plasma column, in O-mode, in the vertical direction (i.e., parallel to the tokamak axis) and a reference beam traveling the same distance in the air. The probing beam of radian-frequency $\omega \gg \omega_{pe}$ has a cutoff density of $n_c = \omega^2 \frac{\epsilon_0 m_e}{e^2}$. After traveling a distance of L in the plasma, the total phase shift (Ref. 4, p. 68),

$$\frac{\Delta\Phi}{2\pi} = \frac{\omega}{4\pi c n_c} \int_0^L n_e(x) dx \quad (7)$$

with respect to the reference beam traveling in the air. This can be used to determine the line integrated density of the plasma column along the line of sight. The local density can be obtained via mathematical inversion using the data obtained from different interferometric LOS. By using two or more probing frequencies, the ambiguity in phase measurements and the misalignment errors of the optical components inside the machine can be removed, increasing the calibration accuracy of the diagnostic.³¹ The **polarimetry** diagnostic makes use of the same interferometry laser beam, exploiting the polarization rotation induced by the plasma birefringence properties after traveling a distance L in plasma. This phenomenon is called the Faraday Effect,⁴

$$\alpha_{Faraday} = \frac{e^3}{2c\epsilon_0 m_e^2} \frac{1}{\omega^2} \int_0^L B_{\parallel} n_e(x) dx \quad (8)$$

B_{\parallel} is the poloidal magnetic field component parallel to the beam path. By measuring $\alpha_{Faraday}$, the convolution between B_{\parallel} and the electron density can be obtained by inversion and then using the density measured along the same line of sight to extract B_{\parallel} . For this purpose, interferometry and polarimetry are often combined in tokamaks in a heterodyne-style detection diagnostic^{1,32} capable of providing all quantities required to extract the magnetic field. In fusion plasmas, the high densities and temperatures make the plasma magnetic fields comparable to the vacuum field,¹⁶ which makes it essential to properly measure these quantities during the discharge. Although compact, the combined scheme requires additional components, such as beam splitters and additional detectors [Fig. 3(a)]. The use of a THz-TDS spectrometer with polarization-resolving detectors and an emitter and receiver located at the opposite ends of a vertical LOS [Fig. 3(b)] will provide a simplified implementation of the two measurements, as shown by the comparison of the two schemes in Fig. 3. Some of the complications of the classic interferometric arrangement, such as splitting the probe beam into two branches (reference and probe) and then detecting them separately, will be eliminated.

Fusion-relevant plasmas have electron densities in the range 10^{18} – 10^{21} m^{−3}, corresponding to plasma frequency between 10 and 280 GHz. The lower part of the THz-TDS spectrum (1–2 THz) satisfies the linearity condition in Eq. (3) and is suitable for diagnostic applications. The successful implementation of this technique will imply the need to rename the diagnostic since the THz-TDS systems are not, strictly speaking, “interferometric.” In addition, because at

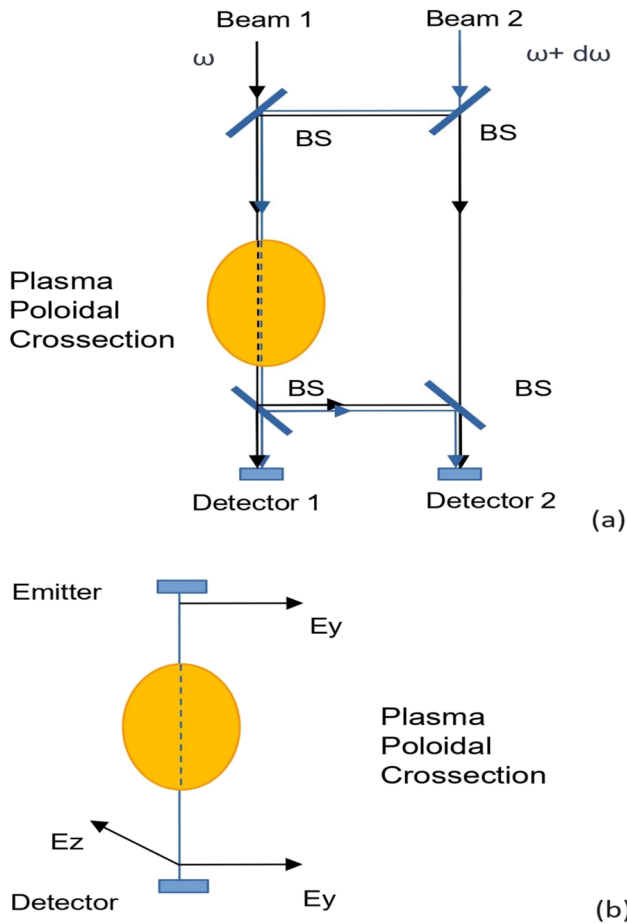


FIG. 3. (a) Principle of a classic heterodyne scheme for simultaneous Faraday rotation and interferometry measurements in tokamaks.¹ (b) Schematic of the same combined measurement with THz-TDS spectrometry and polarization resolving detectors, which provides a simpler layout.

the present time polarimetry is being superseded by the motional Stark effect for local magnetic field measurements, the THz-TDS diagnostic application could potentially determine its resurrection.

Given the optical access limitations to the tokamak vacuum chamber, the plasma refraction must be taken into account to keep the full refractive deviation angle θ_{\max} small enough to not lose the beam in the receiving antenna. Considering a monochromatic wave inside an asymmetric parabolic density profile with central density n_0 , θ_{\max} is given by^{33,34}

$$\theta_{\max} = \frac{n_e}{n_c} = \frac{e^2}{4\pi^2 c \epsilon_0 m_e} n_0 \left(\frac{2\pi c}{\omega} \right)^2. \quad (9)$$

As an example of the order of magnitude of the quantities involved in the diagnostic design, the relevant parameters can be estimated in the simple case of a compact-size tokamak (such as FTU). With a minor radius of $a = 0.3$ m, a major radius of 0.935 m, a plasma electron density of $n_e = 0.5 \times 10^{20} \text{ m}^{-3}$, and a poloidal magnetic field of $B_\theta = 0.1$ T, the refraction index at peak density of 1 THz

probing beam is $N = 0.997$ [Eq. (3)]. The phase shift across the full plasma cross section of $L = 0.6$ m is [Eq. (7)] $\frac{\Delta\Phi}{2\pi} = 4.03$. From Eq. (8) $\alpha_{\text{faraday}} \approx 7$ mrad and from Eq. (9) the maximum refraction angle $\theta_{\max} \approx 4.03$ mrad.

Reflectometry is a technique based on the detection of a microwave beam reflected at the critical density (or cutoff) plasma layer, where the refractive index N vanishes. Inside the layer, the refractive index becomes imaginary and the wave is damped. For the conservation of energy, the wave is reflected.^{1,35} The phase variation of the selected frequency components can be used to diagnose the plasma density profiles or density fluctuations. The details of this technique can be found in the E. Mazzucato review³⁶ and in the seminal Heald and Wharton book.²⁵ A typical reflectometry setup consists of an emitter launching a beam of an appropriate frequency along a horizontal chord on the tokamak equatorial plane and a detector to collect the radiation reflected on the corresponding cutoff layer, as shown in Fig. 1. By using a broad band spectrum probe beam and resolving the phase shift of selected components, the radial density profile can be obtained via Abel inversion. This considers the dispersive effect during propagation across non-zero refraction index plasma layers. The THz-TDS reflectometer is an evolution of the ultrashort pulse radar technique³⁷ but with the broadband spectrum required for the diagnostic obtained through a terahertz switch, with a pulse width of 5 ps rather than a microwave transmitter (a pulse width of 5 ns). It must be noted here that the current THz-TDS technology aims at the higher part of the spectrum (>1 THz). In order to probe the tokamak cutoffs (100–200 GHz, see Fig. 2), the THz emitter and receivers and the optics will have to be tailored to operate at lower frequencies avoiding diffractive losses. This will be easily done by using emitters with larger electrode gaps and apertures.

V. MULTI-FUNCTIONAL THz-TDS DIAGNOSTIC LAYOUT

The prototype diagnostic scheme based on a standard THz-TDS system is discussed here with the help of Fig. 4. The femtosecond laser beam is divided into two sub-beams by a suitable beam splitter: a lower power beam (usually 30%) for the receiver (RX) and the other for the scanning stage, followed by the emitter (TX). The two beams are then coupled from free space into two optical fibers of equal length to reach the RX and TX. The emitter and receiver are GaAs wafers with photo-lithography deposited electrodes, which generate a dipole pattern converted into a Gaussian beam by a Si lens. For tokamaks, additional collimating lenses can be introduced in the optical setup. A suitable material is the Polymethylpentene (Poly-4-methyl-1-pentene),³⁸ often referred to under the trade name TPX[®]. The use of long optical fibers poses the issue of compensating for the Group Velocity Dispersion (GVD) with a suitable compression stage because the initially narrow THz pulse will be broadened by the dispersive properties of the fibers.³⁹ This is discussed later in this study. A single GVD compressor for the two beams is desirable, as it minimizes losses and reduces optical design complexity, but at the same time requires the use of two fibers of identical length, which means introducing a long free-air compensation path in one of the two branches. This is in contrast to the requirement of entering the optical fiber as soon as possible after compression, owing to the unavoidable degradation of the

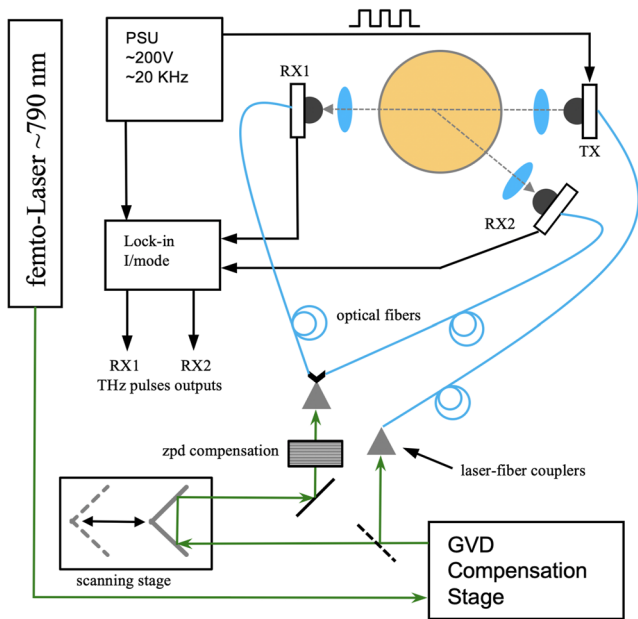


FIG. 4. General schematic of a fiber-optics THz-TDS spectrometer for plasma diagnostics applications, based upon a single GVD compensation stage and a zero path difference (ZPD) compensation on the receiver branch. The emitter TX feeds both receiver RX1 (for polarimetry and interferometry) and receiver RX2 (for reflectometry). The angles between emitter and receiver lines of sight have been exaggerated for graphical clarity. The lock-in amplifier output signal vs the scanner position is the THz pulse.

laser beam that occurs during compression. This is a potential drawback of the fiber coupled system in plasma diagnostics applications because the THz path in plasma (several meters) is part of the TX branch; therefore, to ensure that the TX and RX paths are equal, a long compensation path is required on the receiver branch. The use of two separate compressors with fibers of different lengths would solve this issue. It is advisable to begin with a single GVD compressor and evaluate the results for the final diagnostic design. Classic path-difference scanning based on a translating stage moving a rooftop mirror may not be suitable for the time resolution of tokamak diagnostics. Alternative solutions are helicoidal rotating mirrors that have been successfully tested in ECE diagnostics with millisecond time resolution²⁹ or dual-laser systems, in which the most popular optical ed electronic configurations are asynchronous optical sampling (ASOPS⁴⁰) and electronically controlled optical sampling (ECOPS⁴¹), based on two mode-locked lasers with slightly different pulse repetition rates, to achieve a time scan between the RX and TX without moving optomechanical components.⁴⁰

VI. PLASMA DIAGNOSTICS-RELEVANT EXPERIMENTAL TESTS

The full exploitation of THz-TDS in the vast landscape of plasma diagnostic applications requires a systematic study of each individual measurement to demonstrate its effectiveness in experimental situations as close as possible to the expected ones and to obtain the parameters required for the final diagnostic design.

A. Comparison of photoconductive and electro-optical detection

The photoconductive and electro-optical detection schemes were directly compared using the same spark-gap emitter shown in Fig. 5(a) (identified by the code FR-05) with two different detection systems: the photoconductive GaAs detector in Fig. 5(b) and an electro-optical setup [Fig. 5(c)]. The overall setup is shown in Fig. 5(d). The emitter FR-05 is made of two parallel conductive strips separated by a 400 μm gap, deposited on a 3 mm thick semi-insulating GaAs substrate. It was aligned with the pump laser beam by minimizing the electrical resistance between the strips.²¹ The emitter was polarized with a square-wave modulated voltage

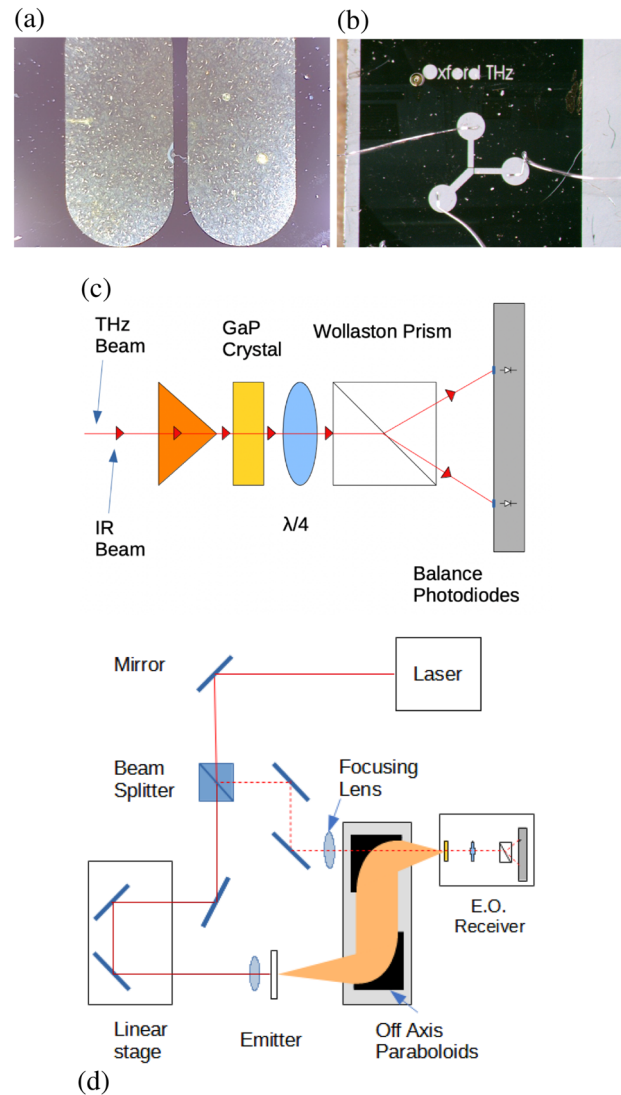


FIG. 5. Photo-conductive and electro-optical detection test: (a) Spark-Gap Emitter, (b) photo-conductive detector, (c) electro-optical detection stage, and (d) full THz setup employing a pair of off-axis parabolic mirrors to couple emitter end receiver. In this scheme, the EO detection stage is shown.

TABLE II. Photo-conductive vs EO measurement parameters. The two setups have different sampling and scan length, hence different cutoff frequency ($= \frac{1}{2} f_{Nyquist}$) and different spectral resolution ($= \frac{1}{2L}$), calculated using Rayleigh criterion, without apodization.³⁰

Detector type	Points per pulse	Sampling rate (ps)	$\frac{1}{2}f_{Nyquist}$ (GHz)	Scan length L (ps)	Spectral resolution (GHz)	TX bias (V)	Modulation frequency (kHz)	Alignment resistance (k Ω)
Photo-conductive	199	0.03	14.92	7	71	120	17	335
Electro-optical	280	0.22	2.24	62	8	200	17	26

(~100–200 V), generating a field of 5 kV/cm across the 400 μm gap, bringing the semiconductor close to the spark emission threshold, which is triggered by the laser pulse electric field. In our case, the optimum resistance obtained during the alignment of the emitter photoconductor was 335 k Ω at 120 V bias voltage and 26 k Ω at 200 V.

The photo-conductive detector (identified as FD-12) is made of three gold electrodes deposited on a 0.4 mm GaAs substrate, with annealing at 600 °C. The gap between the ground (common) contact and each of the two electrodes in the X–Y direction [Fig. 5(b)] was 12 μm . Only one polarization was used for this test, although this arrangement has the potential to simultaneously measure the two polarizations. The gap was aligned with the laser using the same resistance minimization technique used for the emitter. The laser pulse, divided by a beam splitter, enables the detector gap during

the THz pulse, so a current proportional to the THz intensity (electric field) flows in the gap. It was measured using a lock-in amplifier (signal recovery model 7280), set in current mode, with a sensitivity of 2 nA and phase $\phi = 0.47^\circ$ after reset to maximize the X component of the signal.

Electro-optical sampling exploits the variation in birefringence induced in a non-linear medium (GaP crystal with 110 orientation) by the incoming electric field. By measuring the intensity of the two polarizations resulting from birefringence in the crystal (for example, with a pair of balanced photodiodes), the intensity of the THz pulse electric field can be inferred.⁴² The measurement parameters are summarized in Table II.

Data were analyzed using a Python script to calculate the Fast Fourier transform, perform data selection, differentiate when required, smooth, and normalize the spectra. The results, displayed in Fig. 6, show that the shape of the normalized spectra is consistent when the better spectral resolution of the EO system is considered.

B. Tests of pulse compression after optical fiber broadening

As mentioned in Sec. V, ultrashort laser pulses propagating inside optical fibers, given their large frequency bandwidth, suffer major temporal broadening as a consequence of the GVD.³⁹ A reliable estimate of GVD induced by common fused silica fibers (for example, the 780-HP in Table III) after a length L in an 800 nm pulsed laser with bandwidth bw is¹¹

$$\Delta\tau [fs] = 120 \times L [m] \times bw [nm]. \quad (10)$$

The expected widening of a 30 fs laser pulse (corresponding to 100 nm bandwidth) with a fiber length of 5 m is $120 \times 5 \times 100 \sim 60\,000$ fs, which means that THz-TDS generation is impossible. To compensate for this GVD, we tested the widely adopted scheme shown in Fig. 7. With systematic scanning of the distance d , the optimum compression was found for $d = 27$ mm (Fig. 8), obtaining a full width at half maximum (FWHM) of 542 fs, corresponding to a com-

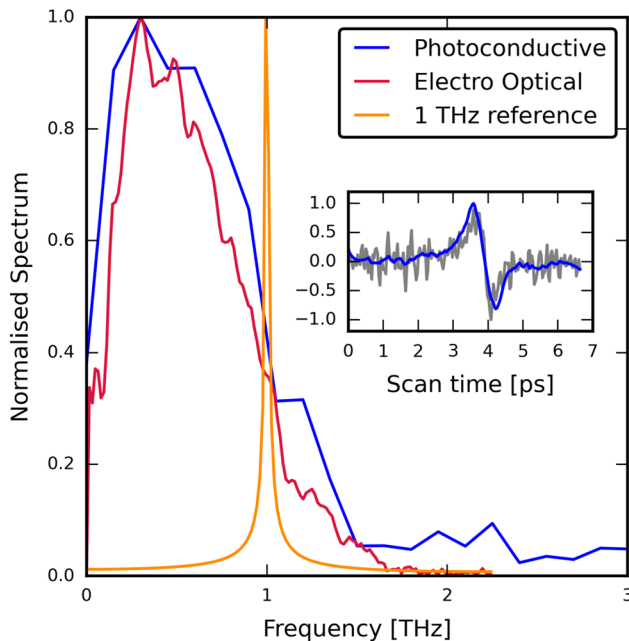


FIG. 6. Comparison of the normalized THz spectrum measured with photoconductive and electro-optical detection methods. The 1 THz reference line has been calculated with numerical sine input on the EO data time base, with the same spectral analysis program used for the experimental data. The photoconductive THz pulse has been smoothed with a Savitzky–Golay digital filter with 31 points of window length and polynomial order = 3. In the inset box, the photoconductive THz pulse before (gray line) and after filtering is displayed.

TABLE III. Characteristics of optical fiber 780-HP.

Quantity	Value or range
Operating wavelength	780–790 nm
Cutoff wavelength	730 ± 30 nm
Core diameter	$2a = 4.0 \mu\text{m}$
Numerical aperture	N/A = 0.14
Refractive index value-core	1.463 @ 651 nm

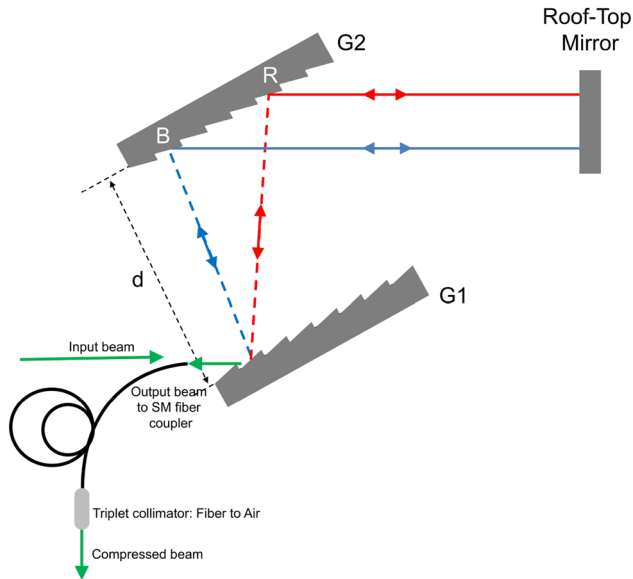


FIG. 7. Schematic of the pulse compression stage tested at Clarendon Laboratory. Two holographic gratings (G1 and G2) Spectrogon 715.700.550 with 1200 grooves/mm and Littrow angle = 27.90° at 780 nm provide the required negative dispersion. The roof top mirrors vertically separate the input and output beams. “Red” and “blue” wavelengths refer to the laser pulse’s lower and higher spectral limits. The output beam is coupled with a single mode optical fiber (Table III) and sent to a Femtochrome FR-103MC autocorrelator for pulse width measurement by using a triplet collimator for fiber–air coupling.

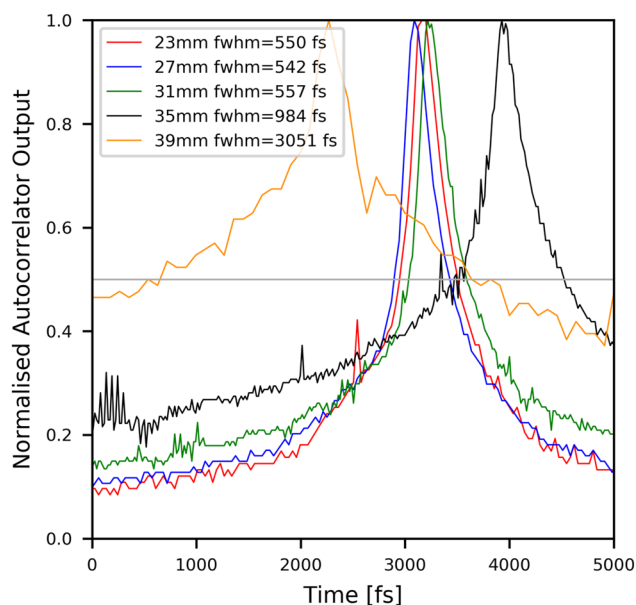


FIG. 8. Normalized laser pulse width measured for different gratings separation d at the output of the compression stage shown in Fig. 7. The horizontal gray line marks 50% signal level. Inset box: FWHM of the pulses. The optimum compression is achieved for $d = 27$ mm.

pression factor of >1000 . This value is consistent with the estimate $d \approx 50$ mm obtained from F. Ellrich paper,¹² while taking into account the different characteristics of the optical fibers and the extra positive dispersion occurring in the system, for example in the triplet collimator and in the gratings glazing. The compressed pulse length achieved in this test (~ 500 fs) is still marginal for THz generation and detection but constitutes good experimental proof of the feasibility of the technique, given the ample optimization margins of the system. In addition, for THz plasma diagnostics we are interested in the lower part of the THz spectrum (below 2 THz) because it will be possible to start with a wider laser pulse (>100 fs), which will result in a narrower spectral band and reduced dispersion; hence less compensation is required.

C. Transmission and refractive index measurement

The measurement of the plasma refractive index is one of the most important purposes of FIR and submillimeter wave plasma diagnostics. As a preliminary evaluation of the practical applicability of this technique on a sample with well-known properties, we used a solid 1 in. diameter disk of 1 mm transverse thickness d , fabricated using a 3D printer from a standard polylactide (PLA) filament. The information obtained will serve as a benchmark for more complex plasma measurements. Transmission properties were measured using a commercial THz-TDS system (Picometrix T-Ray 5000). This system operates with a 100 fs laser pulse carried by optical fibers to a pair of GaAs 4×4 mm² wafers, which act as the emitter and receiver. The THz radiation is focused on the sample by a standard arrangement made of a Si hemispheric lens followed by a TPX lens with an effective 6.5 cm focus length. By describing the electric pulse traversing the sample as $E(\omega)_{smp}$ and the electric field in free air as $E(\omega)_{ref}$ via Fourier transform, it is possible to obtain the transmission spectra $\left| \frac{E(\omega)_{smp}}{E(\omega)_{ref}} \right|$ and the phase difference $\Delta\phi = \arg\left(\frac{E(\omega)_{smp}}{E(\omega)_{ref}}\right)$ between the two measurements. It is possible to obtain a rough estimate of the index of refraction N and the absorption coefficient k using the following equations:⁴³

$$N(\omega) = n_{air} - \frac{c}{d\omega} \Delta\phi(\omega), \quad (11)$$

$$k(\omega) = -\frac{c}{d\omega} \ln\left(\frac{E(\omega)_{smp}}{E(\omega)_{ref}}\right), \quad (12)$$

where n_{air} is the index of refraction in free air and k is the absorption coefficient. A typical measurement is shown in Fig. 9, illustrating how, with a simple algorithm, rather than the Kramers–Kronig relationship⁴⁴ always used in many areas of spectroscopy, THz-TDS makes it possible to retrieve the index of refraction and absorption coefficient from the experimental data, thus providing a full characterization of the optical properties of materials or system elements and components. In Fig. 9, the index of refraction is compatible with values found in the literature,⁴⁵ while our basic estimate of the absorption coefficient suffers of the inaccuracy in the sample thickness d ; hence, the estimated value was found to be a factor 10 lower than the expected.

The plasma density of different arc discharge spectroscopic lamps was measured using THz-TDS.⁴⁶ Using a simple model⁷ of the THz pulse transmission, the plasma electron density n was estimated to be consistent with the spectral characteristics of the lamps.

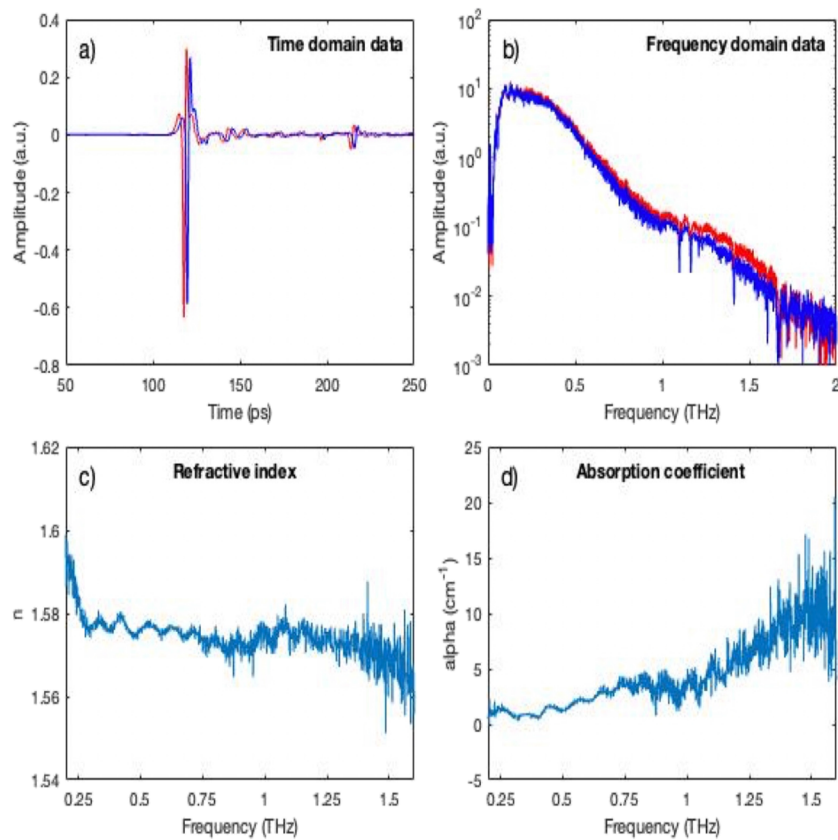


FIG. 9. Measured optical constants of PLA disk: (a) The averaged time evolution of the THz electric field of the reference (red line) and signal (blue line) (1000 THz scans average). (b) Amplitude spectra of the signals obtained by their Fourier transforms. (c) Refractive index and (d) absorption coefficient of the measured sample. The estimated phase noise in this test was $\sim 1^\circ$, quickly increasing above 1 THz.

D. Validation of reflectometry measurements

As detailed in Sec. IV, the aim of reflectometry diagnostics is to locate the position of cutoff reflecting layers. On this basis, an estimate of the attainable reflectometry spatial resolution was made with a series of measurements of stacks of plain paper sheets (from 1 to 4), made with the Picometrix T-Ray 5000 system described in Sec. VI C. A THz beam splitter was inserted between the emission and detection heads, perpendicular to each other. In this scheme, the THz pulse passes through the beam splitter and reaches the reflecting sample. After reflection on the sample, a fraction of the signal will reach the detection head.

The results shown in Fig. 10 are as follows: with one layer there was no measurable difference from the reference pulse, that is, no detectable optical path variation being the refraction index of paper in the THz range between 1.2 and 1.5. The distance between the paper sheets can be estimated from the spacing between the corresponding peaks in the THz pulse, using the propagation time in free air: 0.3 mm in 1 ps. The separation between two sheets estimated with this technique is 0.7 mm for the first two and 1.3 mm for the second. The convolution of the Fabry–Perot étalons maxima was evident in the reflected radiation spectrum (Fig. 10). The

correct understanding of this effect is a key point in plasma diagnostics design, where there are many optical components that can potentially create étalons.

Another demonstration of the potential of this type of measurement was obtained using the same reflectometry system to map, through a 3D scan, the internal structure of a more complex sample (an electronic board), as shown in Fig. 11.

E. Validation of polarimetry measurements using wire grid polarizers

Polarizing optical components based on an inductive grid of metal wires^{47,48} are widely used in FIR plasma diagnostics applications because of their high efficiency in the lower part of the terahertz spectrum. According to Marcuvitz *et al.*⁴⁹ (p. 285), an inductive wire-grid polarizer (WGP) is an infinitely extended grating formed by small metallic obstacles (wires) with axes parallel to the electric field. Alternatively, when the electric field is perpendicular to the wires, the WGP is called capacitive. The WGP parameters are the wire gauge (diameter) (g) and the period of the wire grid (a) (i.e., the spacing between two corresponding parts of the wires). They

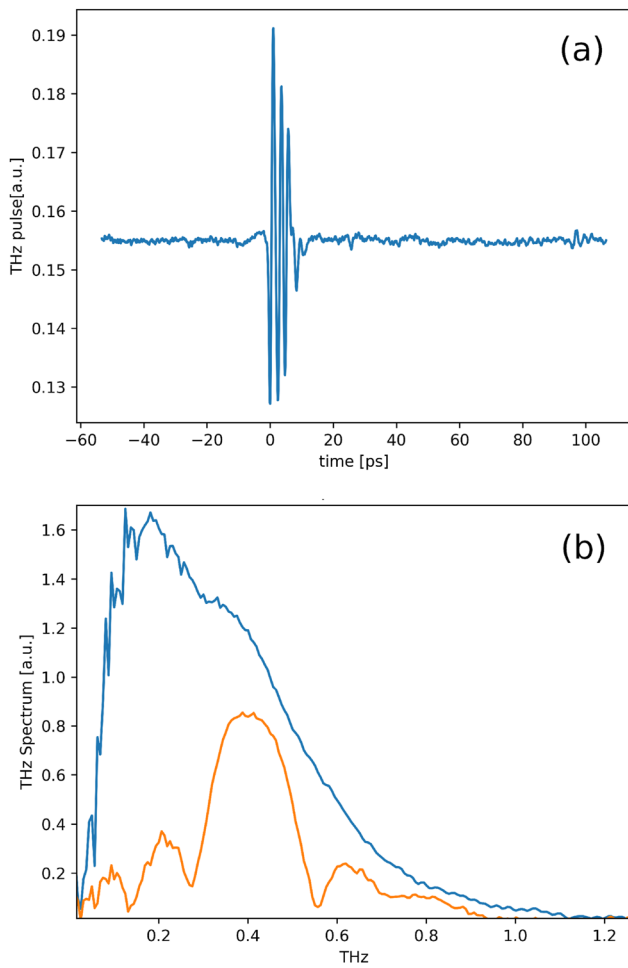


FIG. 10. Reflectometry of a paper sheet stack. The reference spectrum was taken with a metal plate in the same position as the paper stack. (a) Pulse reflected by a stack of four paper sheets. (b) THz spectra of the paper sheets stack (orange line, showing the convolution of Fabry–Perot transmission maxima) and the reference pulse (blue).

define the wire spacing as $d = a - g$. The most important parameter of a WGP is the extinction ratio, which is defined as the ratio of the transmitted power for THz wave polarization perpendicular to the wires in the grid to that parallel to them. For wavelengths larger than the WGP step ($a \ll \lambda$) and a WGP arrangement such that $d \ll a$, the grid acts almost ideally, reflecting waves with an electric field E parallel to the wires and transmitting them when E is perpendicular to the wires. In other words, the extinction ratio is very large. For our tests, we used a standard 1-inch, custom made WGP (QMC Instruments QWG/RT) for plasma diagnostics applications. It was made of free standing tungsten wires of $g = 10 \mu\text{m}$ diameter, equally spaced by $a = 25 \mu\text{m}$ center-to-center. With these parameters, inequality $a \ll \lambda$ translates into $f \ll 12 \text{ THz}$. This is in good agreement with the full transmission spectral response measured with a nanowire detector setup^{50,51} for three relevant orientations of the polarizer, as shown in Fig. 12, which displays a close-to-ideal response up to $\sim 1.5 \text{ THz}$.

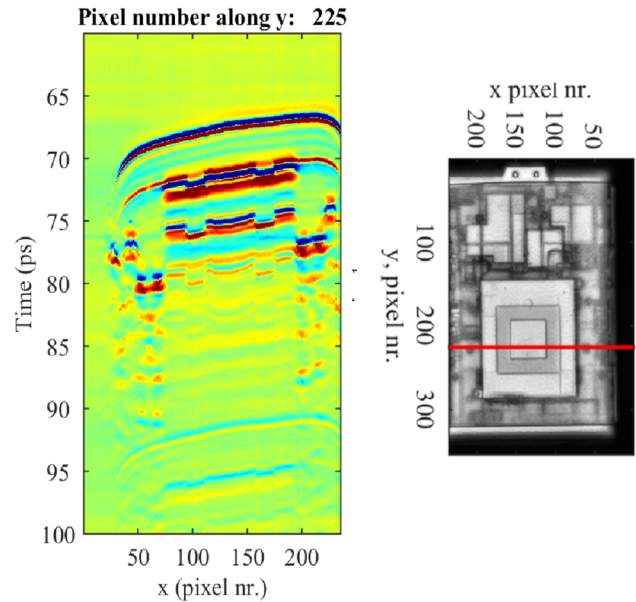


FIG. 11. 3D scan of a commercial electronic board. Left: top view, x = board width, and z = reflection time in ps. The color scale visually maps the intensity of the THz pulse electric field: red (highest positive intensity), yellow (medium), blue (lowest negative intensity), and green (~ 0). The scan is carried out along the x direction, fixing the y coordinate. Right: XY scan of the electronic device, showing the contrast figure of the maximum peak reflections from all the frequencies received and with the red line the scanning path of the adjacent THz pulse map.

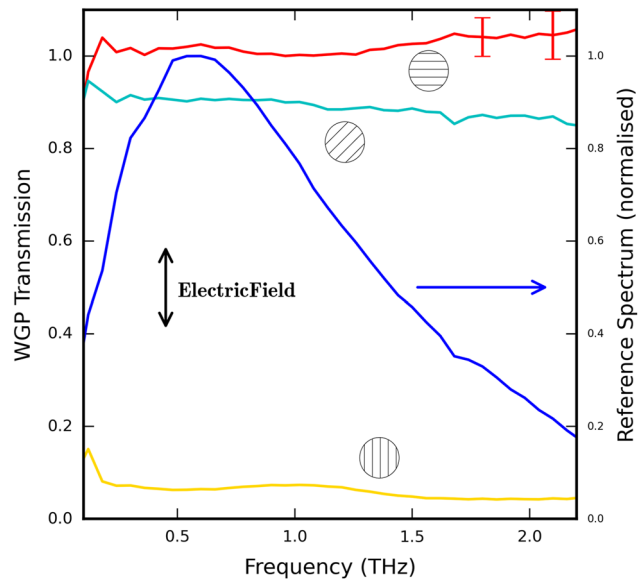


FIG. 12. WGP amplitude transmission in the frequency domain. The THz source is a broadband pulsed spectrum (blue solid line in color version). The spectral response is measured with a nanowire detector with an upper bandwidth limit of 2.2 THz for the three indicated orientations of the wires with respect to a vertically polarized THz beam. The larger error bar causes the apparent transmission > 1 above 2 THz for vertical wire orientation (red trace).

Subsequently, nonlinear transmission and noise become dominant (see caption for details).

The same system was used to determine the extinction ratio of the WGP. Figure 13(a) shows the optical arrangement of this measurement, where a THz pulse passes through the WGP (with vertically oriented wires) and is then collected by the horizontal and vertical channels in the nanowire detector. In the experiment, the polarizer was placed close to the emitter, and the wires orientation was fixed. The incident THz polarization was allowed to rotate from 0° to 90° by rotating the emitter. Figure 13(b) shows the dependence on the emitter rotation angle of the peak-to-peak current in the THz pulse detected by our nanowire detector with and without the wire-grid polarizer inserted in the system. No significant spectral response change was observed with or without the polarizer on the horizontal detection channel (Fig. 13, red line and dots), except for the amplitude transmission ratio; therefore, the broad band measurements made with the THz pulse peak are representative of the response of the component. The accuracy of this basic test setup is $\sim 0.5^\circ$ (9 mrad), and with reasonable technical improvements, the value of 7 mrad required by plasma diagnostics (see Sec. IV) can be easily achieved.

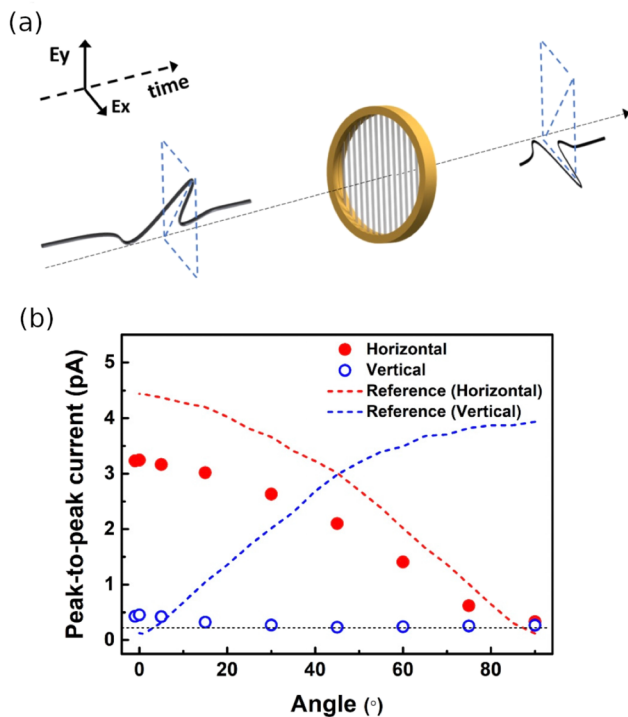


FIG. 13. Characterization of a wire-grid THz polarizer using the polarization-sensitive cross-nanowire detector in THz-TDS. (a) Schematic representation of transmission measurement of a wire-grid THz polarizer (with the grid wires aligned with the y axis). (b) Peak-to-peak responses of the nanowire THz detector as a function of the incident THz polarization angle with (dots) and without (dashed lines) the wire-grid polarizer inserted in the system. (Red): the horizontal detection channel. (Blue): the vertical detection channel. The black dotted line is a guide for the eye.

As expected the transmitted cross-polarized THz radiation detected by the horizontal channel agreed well with the cosine function with respect to the incident THz polarization, whereas the transmitted co-polarized THz radiation detected by the vertical channel was close to zero. The insertion loss of a wire-grid polarizer is defined as the ratio of the transmitted power for THz polarization perpendicular to the wire grids to the transmitted power in the absence of the polarizer. In this case, it was 54%. Furthermore, we observed a small but measurable response signal from the vertical channel when the incident THz polarization was perpendicular to the wire grids. This is due to the leakage of the cross-polarized component of the THz radiation after the polarizer. Such leakage is commonly frequency dependent and increases quickly when the incident THz radiation is above 1 THz, limiting the extinction ratio of the polarizer. The extinction ratio of the WGP was much lower than that of our nanowire detector, which was found to be 40.

VII. CONCLUSION AND FUTURE WORK

The work presented in this article encompasses several years of intensive laboratory research aimed at developing a diagnostic tool for harsh tokamak plasma environments based on THz-TDS technology. To this end, an extensive study of the operational parameters of a THz-TDS plasma diagnostic system was conducted. Interferometry, reflectometry, and polarimetry have been discussed in detail to obtain a full set of instrumental requirements.

Photo-conductive detectors, potentially allowing simultaneous dual-polarization measurements, were studied in depth and compared with a standard THz-TDS electro-optical setup. Valuable experience has been acquired regarding the assembly, alignment, and use of these devices, and the optical arrangement of a plasma diagnostic head working in the Gaussian beam mode has been devised.

Optical fiber operation is essential in plasma diagnostics; hence, we developed and tested a tailored pulse compression stage based on a negative-dispersion grating pair. The device was successfully tested at Clarendon, and an operational set of parameters was defined.

A complementary line of work was developed at the CIO laboratory using commercial equipment with single polarization photo-conductive antennas. The application of this technique to plasma diagnostic measurements have been studied in many cases (polarimetry, refraction index, and reflectometry) to obtain useful insights from techniques performed at the CIO for materials and heritage science.

The last few decades of nuclear fusion research have been dominated by quasi-optical and microwave techniques. Although powerful, while approaching next-generation fusion devices, these techniques start showing some limitations, especially in terms of plasma access, SNR, calibration, and reliability. In this framework, through a series of laboratory tests, we outlined the building blocks of the novel THz-TDS multi-functional plasma diagnostic. To transfer this technique from the laboratory table to the nuclear fusion environment, several key issues will have to be resolved. Neutron emission can affect the hardware near the machine; this is a problem shared with all the plasma facing diagnostics, and the solution developed for it can be applied to THz-TDS as well. Noise induced by mechanical vibrations with loss of alignment (see Sec. IV) is specific to each machine and can be contained with an appropriate

GBM design of the optics. Electrical pickup disturbance is a common issue for detectors, tackled with the appropriate choice of lock-in frequency after *in situ* tests of the noise spectrum.

A powerful network of laboratories has been created, each providing a specific set of skills and techniques. The resulting synergy will be the propulsive force for the final step in the realization of the diagnostic for the next step fusion devices.

ACKNOWLEDGMENTS

We are pleased to thank the people who contributed to this work, particularly M. Johnston for the useful discussions providing advice, encouragement, and continuous support, and for making his Oxford facilities available; E. Castro-Camus for hosting and guiding one of the authors during his Ph.D.; J. Boland for her constructive comments; G. Rocchi and V. Piergotti for precious and continuous technical support; and E. Giovannozzi for his valuable help with Python coding. In no particular order, we acknowledge S. Jones, D. Damry, H. Joyce, J. Lloyd-Hughes, R. Milot, C. Xia, and P. Pattinson.

AUTHOR DECLARATIONS

Conflict of Interest

The authors have no conflicts to disclose.

Author Contributions

G. Galatola Teka: Conceptualization (lead); Data curation (lead); Formal analysis (lead); Funding acquisition (lead); Investigation (lead); Methodology (lead); Project administration (lead); Resources (lead); Software (lead); Supervision (lead); Validation (lead); Visualization (lead); Writing – original draft (lead); Writing – review & editing (lead). **K. Peng:** Data curation (equal); Formal analysis (equal); Investigation (equal); Validation (equal); Visualization (equal); Writing – review & editing (equal). **M. Alonzo:** Conceptualization (equal); Data curation (equal); Formal analysis (equal); Validation (equal); Visualization (equal); Writing – review & editing (equal). **F. Bombarda:** Conceptualization (supporting); Data curation (supporting); Validation (equal); Writing – original draft (equal); Writing – review & editing (equal). **C. L. Koch-Dandolo:** Data curation (equal); Investigation (equal); Validation (equal); Visualization (equal); Writing – review & editing (equal). **L. Senni:** Conceptualization (equal); Data curation (equal); Formal analysis (equal); Validation (equal); Visualization (equal); Writing – review & editing (equal). **A. Taschin:** Conceptualization (equal); Data curation (equal); Formal analysis (equal); Software (equal); Validation (equal); Visualization (equal); Writing – review & editing (equal). **M. Zerbini:** Conceptualization (lead); Data curation (lead); Formal analysis (equal); Funding acquisition (lead); Investigation (equal); Methodology (lead); Project administration (lead); Resources (equal); Software (equal); Supervision (lead); Validation (equal); Visualization (equal); Writing – original draft (lead); Writing – review & editing (lead).

DATA AVAILABILITY

The data that support the findings of this study are available from the corresponding author upon reasonable request.

REFERENCES

- 1 I. H. Hutchinson, *Principles of Plasma Diagnostics* (Cambridge University Press, 2002), pp. 95, 115, 125.
- 2 K. Miyamoto, *Controlled Fusion and Plasma Physics* (CRC Press, 2006).
- 3 L. Pieroni, “Diagnostics of tokamak plasmas by far infrared techniques,” Tech. Rep., CNEN, CNEN Internal Report 77.25/cc, Frascati, 1977.
- 4 H. J. Hartfuss and T. Geist, *Fusion Plasma Diagnostics with mm-Waves* (Wiley-VCH, 2013), Vol. 67, pp. 75, 83, 342.
- 5 M. Zerbini, “Sailing on far infrared and submillimeter waves plasma diagnostics, towards THz-TDS and beyond,” in *2022 47th International Conference on Infrared, Millimeter and Terahertz Waves (IRMMW-THz)* (IEEE, Delft, 2022), pp. 1–4.
- 6 S. P. Jamison, J. Shen, D. R. Jones, R. C. Issac, B. Ersfeld, D. Clark, and D. A. Jaroszynski, “Plasma characterization with terahertz time-domain measurements,” *J. Appl. Phys.* **93**, 4334–4336 (2003).
- 7 B. H. Kolner, R. A. Buckles, P. M. Conklin, and R. P. Scott, “Plasma characterization with terahertz pulses,” *IEEE J. Sel. Top. Quantum Electron.* **14**, 505–512 (2008).
- 8 K. Kang, D. Jang, and H. Suk, “Plasma density measurements using THz pulses from laser-plasmas,” *J. Instrum.* **12**, C11003 (2017).
- 9 D. H. Auston, K. P. Cheung, and P. R. Smith, “Picosecond photoconducting Hertzian dipoles,” *Appl. Phys. Lett.* **45**, 284–286 (1984).
- 10 M. B. Johnston, D. M. Whittaker, A. Corchia, A. G. Davies, and E. H. Linfield, “Simulation of terahertz generation at semiconductor surfaces,” *Phys. Rev. B* **65**, 165301 (2002).
- 11 S. A. Crooker, “Fiber-coupled antennas for ultrafast coherent terahertz spectroscopy in low temperatures and high magnetic fields,” *Rev. Sci. Instrum.* **73**, 3258 (2002).
- 12 F. Ellrich, T. Weinland, D. Molter, J. Jonuscheit, and R. Beigang, “Compact fiber-coupled terahertz spectroscopy system pumped at 800 nm wavelength,” *Rev. Sci. Instrum.* **82**, 053102 (2011).
- 13 F. Causa, M. Zerbini, M. Johnston, P. Buratti, A. Doria, L. Gabellieri, G. P. Gallerano, E. Giovenale, D. Pacella, A. Romano, A. A. Tuccillo, and O. Tudisco, “THz time-domain spectroscopy for tokamak plasma diagnostics,” *AIP Conf. Proc.* **1612**, 121–124 (2014).
- 14 M. Zerbini, F. Bombarda, A. Doria, G. Galatola-Teka, and E. Giovenale, “From FIR and millimeter waves to THz plasma diagnostics applications,” in *2016 41st International Conference on Infrared, Millimeter, and Terahertz Waves (IRMMW-THz)* (IEEE, Copenhagen, 2016).
- 15 B. Kadomtsev, *Tokamak Plasma: A Complex Physical System* (CRC Press, 1993).
- 16 J. Wesson and D. J. Campbell, in *Tokamaks, International Series of Monographs on Physics*, 4th ed. (Oxford University Press, Oxford, England, 2011), Vol. 149.
- 17 A. Thomson and B. Taylor, *Guide for the Use of the International System of Units (SI)* (National Institute of Standards and Technology, Gaithersburg, 2008), edited by NIST.
- 18 M. Tonouchi, “Cutting-edge terahertz technology,” *Nat. Photonics* **1**, 97–105 (2007).
- 19 A. G. Davies, E. H. Linfield, and M. B. Johnston, “The development of terahertz sources and their applications,” *Phys. Med. Biol.* **47**, 3679–3689 (2002).
- 20 K. Peng, P. Parkinson, Q. Gao, N. Jiang, J. L. Boland, Y.-N. Guo, F. Wang, H. Joyce, L. Fu, M. B. Johnston, H. H. Tan, and C. Jagadish, “Single-nanowire photoconductive terahertz detectors,” *Nano Lett.* **15**, 1206–1210 (2014).
- 21 E. Castro-Camus, J. Lloyd-Hughes, M. B. Johnston, M. D. Fraser, H. H. Tan, and C. Jagadish, “Polarization-sensitive terahertz detection by multicontact photoconductive receivers,” *Appl. Phys. Lett.* **86**, 254102 (2005), [arXiv:0510076](https://arxiv.org/abs/0510076) [cond-mat].
- 22 G. Gallot and D. Grischkowsky, “Electro-optic detection of terahertz radiation,” *J. Opt. Soc. Am. B* **16**, 1204 (1999).
- 23 G. Chantry and J. Fleming, “Resolution limits in Fourier transform spectrometry,” *Infrared Phys.* **16**, 655–660 (1976).
- 24 P. R. Bevington and D. H. Robinson, in *Data Reduction and Error Analysis for the Physical Sciences*, 3rd ed. (McGraw-Hill, New York, 2003), Chap. 3, p. 38.
- 25 M. A. Heald and C. B. Wharton, *Plasma Diagnostics with Microwaves* (Wiley, 1965).

- ²⁶R. A. Cairns, *Plasma Physics* (Blackie, Glasgow, 1985).
- ²⁷R. W. Boyd, *Radiometry and the Detection of Optical Radiation* (Wiley, 1983).
- ²⁸M. E. Austin and J. Lohr, "Electron cyclotron emission radiometer upgrade on the DIII-D tokamak," *Rev. Sci. Instrum.* **74**, 1457–1459 (2003).
- ²⁹P. Buratti and M. Zerbini, "A Fourier transform spectrometer with fast scanning capability for tokamak plasma diagnostic," *Rev. Sci. Instrum.* **66**, 4208–4217 (1995).
- ³⁰J. R. Birch and T. J. Parker, "Dispersive fourier transform spectrometry," in *Infrared and Millimeter Waves, Volume 2: Instrumentation* (Academic Press, 1979), Chap. 3, pp. 137–271.
- ³¹A. Canton, P. Innocente, and O. Tudisco, "Two-color medium-infrared scanning interferometer for the Frascati tokamak upgrade fusion test device," *Appl. Opt.* **45**, 9105–9114 (2006).
- ³²G. Dodel and W. Kunz, "A far-infrared 'polari-interferometer' for simultaneous electron density and magnetic field measurements in plasmas," *Infrared Phys.* **18**, 773–776 (1978).
- ³³D. Veron, "Submillimeter interferometry of high-density plasmas," in *Infrared and Millimeter Waves, Volume 2: Instrumentation*, edited by K. J. Button (Academic Press, 1979), Chap. 2, pp. 67–135.
- ³⁴J. Shmoys, "Proposed diagnostic method for cylindrical plasmas," *J. Appl. Phys.* **32**, 689–695 (1961).
- ³⁵G. Bekefi, *Radiation Processes in Plasmas* (Wiley, 1966).
- ³⁶E. Mazzucato, "Microwave reflectometry for magnetically confined plasmas," *Rev. Sci. Instrum.* **69**, 2201–2217 (1998).
- ³⁷S. H. Heijnen, "Pulsed-radar reflectometry: A new approach to measure electron densities in thermonuclear plasmas," Ph.D. thesis, FOM-instituut voor Plasmafysica, 1995.
- ³⁸G. W. Chantry, H. M. Evans, J. W. Fleming, and H. A. Gebbie, "TPX, a new material for optical components in the far infra-red spectral region," *Infrared Phys.* **9**, 31–33 (1969).
- ³⁹J.-C. Diels and W. Rudolph, in *Ultrashort Laser Pulse Phenomena Fundamentals, Techniques, and Applications on a Femtosecond Time Scale*, 2nd ed. (Elsevier/Academic Press, Amsterdam, 2006), Optics and Photonics.
- ⁴⁰A. Bartels, A. Thoma, C. Janke, T. Dekorsy, A. Dreyhaupt, S. Winnerl, and M. Helm, "High-resolution THz spectrometer with kHz scan rates," *Opt. Express* **14**, 430–437 (2006).
- ⁴¹R. Dietz, N. Vieweg, T. Puppe, A. Zach, B. Globisch, T. Göbel, P. Leisching, and M. Schell, "All fiber-coupled THz-TDS system with KHz measurement rate based on electronically controlled optical sampling," *Opt. Lett.* **39**, 6482–6485 (2014).
- ⁴²J. X. Xi-Cheng Zhang, *Introduction to THz Wave Photonics* (Springer, New York, 2009).
- ⁴³W. Withayachumnankul, B. Ferguson, T. Rainsford, S. P. Micken, and D. Abbott, "Simple material parameter estimation via terahertz time-domain spectroscopy," *Electron. Lett.* **41**, 800 (2005).
- ⁴⁴J. D. Jackson, in *Classical Electrodynamics*, 3rd ed. (Wiley, New York, Chichester, 1999).
- ⁴⁵C. H. Brodie, I. Spotts, H. Reguigui, C. A. Leclerc, M. E. Mitchell, J. F. Holzman, and C. M. Collier, "Comprehensive study of 3D printing materials over the terahertz regime: Absorption coefficient and refractive index characterizations," *Opt. Mater. Express* **12**, 3379–3402 (2022).
- ⁴⁶G. Galatola-Teka, "THz-TDS transmission measurements of spectroscopic lamps plasma," in 43rd International Conference on Infrared, Millimeter, and Terahertz Waves (IRMMW-THz). Nagoya, Japan, 2018.
- ⁴⁷A. E. Costley, K. H. Hursey, G. F. Neill, and J. M. Ward, "Free-standing fine-wire grids: Their manufacture, performance, and use at millimeter and submillimeter wavelengths," *J. Opt. Soc. Am.* **67**, 979–981 (1977).
- ⁴⁸A. Sentz, M. Pyee, C. Gastaud, J. Auvray, and J. P. Letur, "Construction of parallel grids acting as semitransparent flat mirrors in the far infrared," *Rev. Sci. Instrum.* **49**, 926–927 (1978).
- ⁴⁹N. Marcuvitz, *Waveguide Handbook* (McGraw-Hill, New York, 1951).
- ⁵⁰K. Peng, D. Jevtics, F. Zhang, S. Sterzl, D. A. Damry, M. U. Rothmann, B. Guilhabert, M. J. Strain, H. H. Tan, L. M. Herz, L. Fu, M. D. Dawson, A. Hurtado, C. Jagadish, and M. B. Johnston, "Three-dimensional cross-nanowire networks recover full terahertz state," *Science* **368**, 510–513 (2020).
- ⁵¹K. Peng *et al.*, "Direct and integrating sampling in terahertz receivers from wafer-scalable InAs nanowires," *Nat. Commun.* **15**, 103 (2024).